

# Global warming at near-constant relative humidity further supported by recent in situ observations

Herve Douville (✉ [herve.douville@meteo.fr](mailto:herve.douville@meteo.fr))

Météo-France <https://orcid.org/0000-0002-6074-6467>

Saïd Qasmi

Météo-France

Aurélien Ribes

Météo-France

Olivier Bock

ENSG-Géomatique <https://orcid.org/0000-0001-5980-938X>

---

## Article

### Keywords:

**Posted Date:** May 16th, 2022

**DOI:** <https://doi.org/10.21203/rs.3.rs-1616912/v1>

**License:** © ⓘ This work is licensed under a Creative Commons Attribution 4.0 International License.

[Read Full License](#)

---

**Version of Record:** A version of this preprint was published at Communications Earth & Environment on October 10th, 2022. See the published version at <https://doi.org/10.1038/s43247-022-00561-z>.



20 **Although global warming is expected to occur at approximately constant  
relative humidity, the latest IPCC report remains elusive about the magni-  
tude of observed changes in global mean total precipitable water (GTPW)  
and their attribution. Here we use a novel quality-controlled dataset of *in  
situ* observations, global reanalyses, and a long record of global mean  
25 surface temperature (GMST) to constrain both recent and future changes  
in GTPW. Most state-of-the-art global climate models tend to exaggerate  
the projected atmospheric moistening, in line with their overestimation of  
global warming and of the GTPW sensitivity to both anthropogenic green-  
house gases and aerosols across the 20<sup>th</sup> century. A 39% narrowing in  
30 the range of GTPW projections is obtained after applying the observa-  
tional constraints, with a best-guess estimate of 7% per °C of global warm-  
ing. This finding provides further evidence of a substantial intensification  
of the global water cycle as long as GMST is not stabilized.**

Global warming is expected to intensify the global water cycle<sup>1,2,3</sup>, including the  
35 magnitude of heavy precipitation and related extremes<sup>3,4,5</sup>. This adverse hydro-  
logical response is grounded in the Clausius-Clapeyron (CC) relationship,  
which indicates that the water holding capacity of air increases by about 7% per  
1°C of warming, at least in the lower troposphere where most of the atmos-  
pheric water vapour resides. Moreover, global warming is generally assumed  
40 to occur at near-constant relative humidity<sup>2,6</sup>. In other words, a common hypoth-  
esis is that CC does not only control the size of the atmospheric water reservoir  
but also its content on climate change timescales. As a result, water vapour  
changes represent a major positive feedback in climate projections and can  
thus contribute to the inter-model spread in climate sensitivity<sup>7,8</sup>. Water vapour  
45 also controls the horizontal moisture transport and, thereby, the global water  
cycle intensity<sup>1,2</sup> and related precipitation extremes<sup>3,4</sup>. While all global climate  
models support the constant relative humidity hypothesis, they still disagree on  
the quantitative water cycle response to anthropogenic radiative forcings<sup>3,7</sup>,  
which may challenge their ability to predict accurately the GTPW response to  
50 global warming. Their limited horizontal resolution for instance requires the use  
of empirical sub-grid parametrizations which can be responsible for model bi-  
ases but also for contrasted hydrological sensitivities. More importantly, the the-  
oretical expectation of a global warming at constant relative humidity is still lack-  
ing an unequivocal observational evidence.

55

Total precipitable water or the total column of water vapour is defined as the  
mass of water vapour in an atmospheric column over a unit area ( $\text{kg/m}^2$ ). While  
GTPW is a relevant indicator of climate change, global atmospheric reanalyses

do not show fully consistent variations due to the use of evolving satellite data  
60 and the lack of homogeneity in the assimilated observations<sup>9</sup>. Several satellite  
missions have been launched to provide a quasi-global assessment of total  
precipitable water, but failed to provide consistent trend estimates despite an  
overall tropical moistening on top of the strong influence of the El Niño Southern  
Oscillation variability. Most products exhibit apparent breakpoints, which are  
65 generally coincident with changes in the observing system<sup>9</sup>. Even the most re-  
cent reanalyses, such as the ECMWF Retrospective Analysis (ERA5) and the  
NASA Modern-Era Retrospective Analysis for Research and Applications ver-  
sion 2 (MERRA-2) still suffer from spurious water cycle shifts, not only due to  
new observations of specific humidity<sup>9</sup> but also to changes in the surface-wind-  
70 observing system<sup>10</sup>.

Since 2010, the Global Climate Observing System (GCOS) declared the total  
column water vapour to be an essential climate variable and emphasized the  
need of long and homogeneous time series for the detection and attribution  
75 (D&A) of both local and global changes. Yet, only few formal D&A studies have  
been published so far regarding the recent increase in atmospheric humid-  
ity<sup>11,12,13</sup>. The only formal study on the vertically-integrated water vapour con-  
tent was based on the third generation of global climate models (CMIP3) and a  
relatively short (1988-2007) satellite record of microwave measurements above  
80 ocean only<sup>11</sup>. The focus has been also on land surface humidity<sup>13</sup>, with a sug-  
gested underestimation of the observed drying in most previous-generation  
GCMs<sup>14</sup>. The lack of reliable observational evidence has hampered recent pro-  
gress in the assessment of GTPW trends from the fifth to the sixth Assessment

Report of the IPCC. The AR5 concluded that total column water vapour *very*  
85 *likely* increased since the 1970s at a rate that is overall consistent with the CC  
relationship (about 7%/°C), and that an anthropogenic contribution to increases  
in specific humidity was found with *medium confidence* at and near the surface.  
The AR6<sup>7</sup> was even more cautious, stating only that (it is *likely* that) human  
influence has contributed to moistening in the upper troposphere since 1979<sup>15</sup>.

90

Here, and for the first time to the best of our knowledge, we use a novel quality-  
controlled dataset of *in situ* measurements to constrain the projections of  
GTPW in two generations of global climate models (GCMs). Since the early  
1990s, ground-based measurements from the Global Navigation Satellite Sys-  
95 tems (GNSS) have been shown to enable the estimation of total-column water  
vapour by applying the technique of accurate positioning<sup>16</sup> (see Methods). They  
complete the global radiosonde observations and provide an alternative and  
potentially more reliable reference for the evaluation of satellite retrieval algo-  
rithms and of global atmospheric models<sup>17,18</sup>. GNSS measurements are not  
100 sensitive to weather conditions and are performed with high temporal resolu-  
tions (typically a few minutes). The technique consists in the retrieval of the  
vertically integrated water vapour column from propagation delay measure-  
ments. It is relatively insensitive to instrumentation changes and is thus suitable  
for trend assessments<sup>19</sup>.

105

The present study takes advantage of a recently updated GNSS dataset<sup>20</sup>  
based on a network of 434 stations with more or less continuous measurements  
from January 1994 to December 2021. These stations exhibit globally averaged

anomalies that are consistent with the global mean values derived from several  
110 state-of-the-art atmospheric re-analyses over recent decades (Fig. 1). Yet, the  
estimated linear trend since 1994 remains data-dependent, with ERA5 showing  
a slightly stronger global moistening ( $+0.39 \text{ kg m}^{-2} \text{ decade}^{-1}$ ) than GNSS ( $+0.34$   
 $\text{kg m}^{-2} \text{ decade}^{-1}$ ) and the other two re-analyses ( $+0.32$  and  $+0.33 \text{ kg m}^{-2} \text{ dec-}$   
115  $\text{ade}^{-1}$ ). The 20<sup>th</sup> century re-analyses from ECMWF (ERA20C<sup>21</sup>) is fairly con-  
sistent with the other products, although it only assimilates surface pressure  
and surface wind measurements. This result indicates that GTPW is strongly  
constrained by the prescribed observed sea surface temperature (SST) bound-  
ary conditions. It also suggests that the pre-1994 stalling of GTPW found in  
ERA5, MERRA-2 and JRA55 is likely an artifact of changes in the observation  
120 system. For this reason, we will only use the 1994-2021 observation period to  
constrain the climate projections. ERA20C will not be used as a direct observa-  
tional constraint, but will be used indirectly (via a simple regression technique,  
see Methods) to derive GTPW anomalies from the observed variations in global  
mean surface air temperature (GSAT).

125

Beyond observations and reanalyses, the latest-generation GCMs from CMIP6  
can be also used to document and better understand the historical evolution of  
GTPW (Fig. 2). Four multi-model ensembles of 1850-2020 simulations  
achieved in the framework of the DAMIP project<sup>22</sup> can be compared: hist-NAT  
130 (natural forcings only), hist-GHG (anthropogenic greenhouse gases only), hist-  
AER (anthropogenic aerosols only), and hist-ALL (all historical forcings, also  
including a few other forcings in some but not all models, such as land-use  
change). Only eight CMIP6 models providing a minimum of three realizations

for each experiment have been considered (see Methods). The hist-ALL ensemble shows an overall increase in GTPW since the mid-19<sup>th</sup> century, which is broadly consistent with the poorly constrained ERA20C reanalysis. Remarkably, the simulated increase is much stronger after the mid-1980s, and is quite consistent with the GNSS measurements from 1994 to 2021. This result suggests a significant influence of the anthropogenic emissions of sulphate aerosols, which peaked in the mid-1980s before declining at the global scale<sup>3,7</sup>.

Parallel historical experiments with individual radiative forcings confirm this hypothesis. The 20<sup>th</sup> century GTPW response is mainly the combination of a strong water cycle sensitivity to both GHG and AER forcings, with the latter damping the atmospheric moistening caused by GHG emissions. Compared to human activities, natural forcings (i.e., solar activity and volcanic eruptions) and internal variability (as assessed from the multi-member ensembles) only had a marginal influence. The key role of anthropogenic aerosols in damping the early GTPW response to GHG is consistent with our current understanding of the water cycle sensitivity<sup>3,23</sup>. Similar conclusions have been drawn for the response of GSAT<sup>24</sup>, in line with the AR6 highlighting that the observed global warming of ~1.1°C since the late 19<sup>th</sup> century is unequivocally attributable to a human influence<sup>15,24</sup>.

While the ensemble-mean response of the subset of eight CMIP6 models is quite consistent with the GNSS measurements, there is a substantial range of historical responses across individual models (cf. shading in Fig. 2). The spread is even more pronounced in 21<sup>st</sup> century projections, where much more models

can be used to assess future changes in GTPW. Our focus is first on the SSP2-  
160 4.5 scenario whose early GHG emissions are fairly consistent with the observed  
trends. All projections (2015-2100) have been concatenated to their corre-  
sponding historical simulations (1850-2014). GSAT and GTPW annual anoma-  
lies have been estimated against the 1995-2014 baseline period and show a  
substantial range across the 21<sup>st</sup> century (Fig. SM1a and b). Beyond the raw  
165 CMIP6 model distribution, another range of GTPW responses has been derived  
by assuming that all models follow a simple CC scaling (see Methods). This  
scaling is obtained by regressing the anomalies of  $\ln[\text{GTPW}]$  onto the corre-  
sponding anomalies of GSAT. The regression fit is first estimated on simulated  
annual mean anomalies over the 1900-2010 period (Fig. SM1c). The predicted  
170 range and ensemble mean match the raw GTPW distribution, thereby confirm-  
ing that most CMIP6 models comply with this simple scaling. An ERA20C-con-  
strained regression coefficient ( $7.8\%/^{\circ}\text{C}$ ) can be then estimated over the same  
period, and used to predict the simulated GTPW anomalies from the global  
warming of each CMIP6 model (Fig. SM1d). This empirical constraint leads to  
175 an upward shift of the projected distribution, which can be explained by a lower  
ensemble mean regression coefficient ( $6.9\%/^{\circ}\text{C}$ ) in the CMIP6 models over the  
same training period. This result should be however considered with great cau-  
tion for at least three reasons: i) the assumed time-scale invariance of the  
GTPW-GSAT relationship, ii) the limited observational constraint on this rela-  
180 tionship in ERA20C, and iii) the unexplained<sup>22</sup> stronger global moistening in  
ERA20C compared to the same free-running numerical prediction model only  
driven by prescribed SST and radiative forcings (the so-called ERA20CM en-  
semble<sup>21</sup>).

185 Recently, an original statistical method inspired by data assimilation has been developed to narrow uncertainty on simulated estimates of past and future human-induced global warming<sup>24</sup>, as estimated from the increase in global mean surface air temperature (GSAT). The method has also been used at the regional scale<sup>24</sup> and tested successfully in a perfect model framework<sup>24,25</sup>. This robust  
190 statistical approach called KCC (Kriging for Climate Change) uses CMIP projections to provide a *prior* of the real-world forced response and then derive the *posterior* of this response given the historical observations (see Methods). Model uncertainty is fully considered and the entire observational record is used to constrain past and future responses to natural and anthropogenic forcings in  
195 a consistent way. Moreover, the method has been enriched in order to enable the use of two observational constraints while accounting for their potential co-variability<sup>25</sup>. Here, we consider constraints by GMST (a blending of surface air temperature measured over land and of sea surface temperature measured over the oceans, which can be considered as good surrogates for GSAT) and/or  
200 by global mean estimates of total-column water vapour (GTPW) from GNSS and three reanalyses respectively.

Constraining the projected GTPW response using KCC (Fig. 3) leads to a substantial narrowing of the *posterior* compared to the *prior* distribution. Note that  
205 KCC only aims at constraining the forced GTPW response. Unlike more empirical emergent constraints<sup>14,26</sup>, the method thus explicitly discards the contribution of internal climate variability. The constraint is first based either on GMST observations since 1850 (Fig. 3a) or on GTPW observations since 1994 (Fig.

3b). In sharp contrast with the regression technique (Fig. SM1d), KCC leads to  
210 a downward shift of the ensemble mean response, together with a significant  
reduction of the 5-95% confidence interval by 34% and 10% respectively. Com-  
bining the two observational constraints (Fig. 3c) shows that they are not fully  
redundant (despite the full consideration of their co-variability) since the *poste-  
rior* distribution is then narrowed by up to 39% at the end of the 21<sup>st</sup> century. All  
215 constraints lead to a *posterior* ensemble mean forced response that is very  
close to the rate obtained after applying a simple CC scaling of 7%/°C to the  
ensemble mean *posterior* estimate of the forced GSAT response.

This rate of 7%/°C is also consistent with the best estimate of both observed  
220 and KCC-constrained trends over recent decades (Fig. 4). The KCC results  
clearly show that all CMIP6 models do not agree with this best estimate. From  
1994 to 2021, the unconstrained 5-95% confidence interval of the rate of in-  
crease in GTPW ranges from 6.2%/°C to 7.8%/°C, while the constrained confi-  
dence interval is between 6.5%/°C and 7.6%/°C, with a median value of  
225 7.0%/°C. KCC also indicates that the GTPW and GMST observational con-  
straints are quite redundant given the strong relationship between GSAT and  
GTPW trends across the CMIP6 models. Yet, the limited but significant inter-  
model spread in the rate of increase in GTPW as a function of global warming  
explains why the observational constraint from the GNSS measurements (and  
230 from global reanalyses) can represent an added-value compared to the use of  
GMST only. It is therefore important to maintain the GNSS network, which will  
be increasingly useful to constrain the projections of GTPW.

Given the much longer GMST record compared to the four GTPW datasets, an  
235 alternative strategy could consist in combining the KCC method, to constrain  
the GSAT response only, and the simple regression technique, to derive the  
forced GTPW response from the constrained forced GSAT response. Unlike in  
Fig. SM1d, the regression is now based on the GMST-constrained forced GSAT  
response (via KCC) rather than the full GSAT anomalies. A best-guess regres-  
240 sion coefficient of  $7.0\%/^{\circ}\text{C}$ , derived from the GMST and GNSS annual mean  
anomalies over the 1994-2021 overlapping period, is now applied to each  
CMIP6 model. This regression method is however less powerful than KCC for  
constraining the projections (Fig. 3d). This is due to a weak but significant anti-  
correlation between the GSAT response and the rate of increase in GTPW  
245 across the CMIP6 models (Fig. SM2d).

The ensemble mean results of KCC provide an unequivocal demonstration that  
anthropogenic global warming occurs at near-constant relative humidity. Fur-  
ther exploration of the behaviour of individual CMIP6 models at the end of the  
250 21<sup>st</sup> century (Fig. SM2c) shows that all models project an exponential rate of  
increase of GTPW that is around  $7\%/^{\circ}\text{C}$  when normalized by the corresponding  
increase in GSAT. The ensemble-mean rate of increase ( $6.95\%/^{\circ}\text{C}$ ) is similar  
in CMIP5 models (not shown), but hides some model disparity with extreme  
values of  $6.1\%/^{\circ}\text{C}$  and  $7.9\%/^{\circ}\text{C}$  respectively. Note that there is no reason why  
255 the rate of increase should be exactly  $7\%/^{\circ}\text{C}$  after averaging both precipitable  
water and surface temperature at the global scale. For instance, deviations from  
CC scaling of zonal-mean rather than global-mean precipitable water has been  
shown to result from decreases in relative humidity in the subtropics and mid-

latitudes, and increases in the deep tropics<sup>6</sup>. Our subset of CMIP6 models projects a maximum absolute increase in precipitable water in the tropics (Fig. SM3a), where contrasted temperature biases<sup>27</sup> may contribute to the inter-model spread in the estimated moistening rates given the sensitivity of the CC relationship to the background temperature. In contrast, the relative increase in precipitable water (Fig. SM3b) is maximum in the polar latitudes, but should not much contribute to the inter-model spread in GTPW changes given the much lower absolute values of specific humidity. Further investigation is however needed to identify the latitudes or regions that contribute the most to the inter-model spread. Changes in the vertical profiles of temperature and specific humidity should be also explored<sup>28</sup>, including in the tropical upper troposphere where the model response to global warming was shown to be closely related to the model climatology<sup>29</sup>.

A potential weakness of the present study is the simple use of a single realization of the historical experiment and corresponding SSP2-4.5 scenario for each CMIP6 model. However, the use of at least three members (but only 19 instead of 28 models) leads to consistent results (Fig. SM4). Parallel computations have been also made using the SSP5-8.5 scenario from CMIP6 (Fig. SM5) or the RCP8.5 scenario from CMIP5 (Fig. SM6). Again, the KCC method leads to a narrowing and downward shift of the *posterior* distribution compared to the *prior*, with an ensemble mean response fully consistent with the CC relationship. Yet, the regression technique is more efficient with the CMIP5 models that do not show the previously discussed anti-correlation between the rate of increase in GTPW per °C and the GSAT response.

285 To sum up, the KCC statistical package has allowed us to constrain the climate  
projections of GTPW using two observational constraints, without assuming any  
analytical relationship between GTPW and GSAT, and taking account of both  
model and observational uncertainties. The resulting narrowing of the 5-95%  
confidence interval in the forced GTPW response is robust and found in two  
290 scenarios and two generations of GCMs. The KCC method also reduces the  
ensemble mean response, which then matches a 7%/°C rate of increase and  
provides further evidence of a human-caused global warming at near-constant  
relative humidity. This finding is also supported by the D&A experiments from  
CMIP6, which show a consistent historical moistening dominated by GHG emis-  
295 sions but damped by anthropogenic aerosols over much of the 20<sup>th</sup> century.  
Interestingly, KCC is also useful to constrain the historical GTPW response to  
individual radiative forcings (Fig. SM7). While the opposite response to GHG  
versus anthropogenic aerosols (Fig. 2) is confirmed, KCC shows that the over-  
estimation of the projected increase in GTPW is associated with a too strong  
300 sensitivity to both GHG and aerosols. This result highlights the possible adverse  
effect of model tuning: the model ability to capture observed changes is not a  
full guarantee to provide reliable projections if the relative contributions of GHG  
and aerosol forcings vary in time or have not been correctly estimated over the  
historical period<sup>30</sup>.

305

## **METHODS SUMMARY:**

### **Observations and atmospheric reanalyses:**

310 The ground-based GNSS total-column water vapour (or total precipitable water) data used in this work are based on a homogeneous reprocessing of a global network of 434 GNSS stations for the period 1994-2014, extended with a consistent operational processing solution for the period 2015-2021. The basic GNSS product is the Zenith Tropospheric Delay (ZTD) available with a temporal sampling of 2 hours. The ZTD data were thoroughly quality-checked and converted to total precipitable water using ERA5 6-hourly pressure level data, with high horizontal resolution ( $0.25^{\circ} \times 0.25^{\circ}$ ), and aggregated to daily and monthly values. More information on the data processing and conversion can be found in ref [20] (Bock, 2022). The global average time series shown in Fig.1 includes 237 representative sites with more than 10 years of observations. Gaps in the GNSS time series were filled with ERA5 values to insure consistent temporal representativeness. Some differences with the reanalyses shown in Fig. 1 can arise from spatial representativeness differences as the reanalyses are full global averages. These reanalyses differ in the type of observations assimilated: ERA20C assimilates only surface pressure and marine wind observations, while ERA5, JRA55, and MERRA-2 assimilate a huge amount of conventional and satellite data (millions per day). Finally, a recent update of the HadCRUT5 dataset (<https://www.metoffice.gov.uk/hadobs/hadcrut5/>), covering the 1850-2021 period, is used to constrain the evolution of the global mean surface air temperature (GSAT). This dataset is a blending of surface air temperature measured over land and of sea surface temperature measured over the oceans (hereafter called GMST). While the AR6 suggested that the increase in GSAT is slightly higher than in GMST over the historical period, such a limited difference is not reliable across multiple CMIP6 models so that no correction has been here applied to compare the simulated GSAT with the observed GMST.

### CMIP5 and CMIP6 multi-model ensembles:

335 We make use of a large set of global climate models from both CMIP5 and CMIP6. We took  
all models providing at least one historical simulation and a corresponding scenario (SSP2-  
4.5 and SSP5-8.5 for CMIP6, only RCP8.5 for CMIP5) for both *tas* and *prw* monthly mean  
variables, corresponding to near-surface air temperature and total precipitable water respec-  
tively. As a result, we considered twenty-eight CMIP6 models for the SSP2-4.5 intermediate  
340 emission scenario (ACCESS-CM2, ACCESS-ESM-1-5, BCC-CSM2-MR, CanESM5, CESM2-  
WACCM, CNRM-CM6-1, CNRM-CM6-1-HR, CNRM-ESM2-1, EC-Earth3, EC-Earth3-CC, EC-  
Earth3-Veg, EC-Earth3-Veg-LR, FGOALS-g3, GFDL-CM4, GFDL-ESM4, GISS-E2-1-G,  
HadGEM3-GC31-LL, INM-CM4-8, INM-CM5-0, IPSL-CM6A-LR, KACE-1-0, MIROC-ES2L,  
MIROC6, MPI-ESM1-2-HR, MPI-ESM1-2-LR, MRI-ESM2-0, NorESM2-MM, UKESM1-0-LL),  
345 and two more models (HadGEM3-GC31-MM and NorESM2-LM) for the SSP5-8.5 high-emis-  
sion scenario. Alternatively, we also used a subset of nineteen CMIP6 models with at least  
three realizations. For the detection-and-attribution analysis, we considered a smaller subset  
of eight CMIP6 models (ACCESS-ESM-1-5, BCC-CSM2-MR, CanESM5, CNRM-CM6-1,  
GFDL-ESM4, HadGEM3-GC31-LL, IPSL-CM6A-LR, MRI-ESM2-0) providing at least three re-  
350 alizations for the following four experiments: hist-ALL (historical simulations with all natural  
and anthropogenic forcings), hist-GHG (simulations driven by evolving GHG concentrations  
only), hist-AER (simulations driven by evolving anthropogenic aerosol loadings only), and  
hist-NAT (simulations driven by evolving solar and volcanic forcings only). Historical simula-  
tions and the corresponding RCP8.5 high-emission scenario from twenty-eight CMIP5 models  
355 (bcc-csm1-1-m, BNU-ESM, CanESM2, CCSM4, CESM1-CAM5, CMCC-CM, CMCC-CMS,  
CNRM-CM5, CSIRO-Mk3-6-0, FIO-ESM, GISS-E2-H, GISS-E2-H-CC, GISS-E2-R, GISS-E2-  
R-CC, HadGEM2-ES, inmcm4, IPSL-CM5A-LR, IPSL-CM5A-MR, IPSL-CM5B-LR, MIROC5,  
MIROC-ESM, MIROC-ESM-CHEM, MPI-ESM-LR, MPI-ESM-MR, MRI-CGCM3, MRI-ESM1,  
NorESM1-M, NorESM1-ME) have been also used. All model outputs have been retrieved  
360 from the IPSL ESPRI platform (<https://mesocentre.ipsl.fr/plate-forme-physique/>). Annual mean  
anomalies have been estimated relative to the 1995-2014 baseline reference period, as in the  
latest IPCC report.

### **The simple CC scaling:**

365 The objective is to derive changes in GTPW from changes in GSAT. Inspired by the Clausius-  
Clapeyron (CC) relationship, this scaling is obtained by regressing the annual mean anomalies  
of  $\ln[\text{GTPW}]$  onto the corresponding annual mean anomalies of GSAT. The assumption of an  
exponential dependence of GTPW on temperature is not quite correct for finite rather than small  
changes in GSAT<sup>5</sup> and for global mean rather than local values, but it is assumed to be ade-  
370 quate to capture the leading-order sensitivity of GTPW to GSAT. This scaling means that we  
do not use a linear rate to characterize the relative increase in GTPW per 1°C of global warming,  
but rather an exponential rate as previously proposed to quantify relative changes in the inten-  
sity of daily precipitation extremes<sup>5</sup>. This rate of increase is derived as follows:

$$R = (\Delta\text{GTPW}/\text{GTPW} + 1)^{1/\Delta\text{GSAT}} - 1$$

375 where  $\Delta\text{GTPW} / \text{GTPW}$  denotes the fractional changes in GTPW and  $\Delta\text{GSAT}$  denotes the  
GSAT anomalies. Note that we do not account for uncertainties in the coefficient of the linear  
regression  $\ln[\Delta\text{GTPW}] \sim \Delta\text{GSAT}$  when we use this regression to predict changes in GTPW.

### **The KCC (Kriging for Climate Change) statistical method:**

380 The observational constraint method, called Kriging for Climate Change (KCC), has been pre-  
viously applied to global mean warming<sup>24</sup> and regional warming<sup>25</sup>, and can be easily derived  
for other climate variables. This technique consists of three steps. First, the forced response  
of each climate model is estimated over the whole 1850-2100 period (after concatenation of  
historical simulations with corresponding 21<sup>st</sup> century projections). In order to also get attribu-  
385 tion statements, the responses to ALL (all forcings), NAT (natural forcings only) and GHG  
forcings are estimated separately. Second, the sample of the forced responses from available  
climate models is used as a prior of the real-world forced response, assuming that “models  
are statistically indistinguishable from the truth”. Third, observations are used to derive a *pos-  
terior* distribution of the past and future forced response given observations. This Bayesian  
390 method can be summarised using the following equation:

$$\mathbf{y} = \mathbf{H}\mathbf{x} + \boldsymbol{\varepsilon},$$

where  $\mathbf{y}$  is the time-series of observations (a vector),  $\mathbf{x}$  is the time-series of the forced response (a vector),  $\mathbf{H}$  is an observational operator (matrix),  $\boldsymbol{\varepsilon}$  is the random noise associated with internal variability and measurement errors (a vector), and  $\boldsymbol{\varepsilon} \sim N(0, \boldsymbol{\Sigma}_y)$ , where  $N$  stands for the multivariate Gaussian distribution. Climate models are used to construct a *prior* on  $\mathbf{x}$ :  $\pi(\mathbf{x}) = N(\boldsymbol{\mu}_x, \boldsymbol{\Sigma}_x)$ . Then the *posterior* distribution given observations  $\mathbf{y}$  can be derived as  $p(\mathbf{x}|\mathbf{y}) = N(\boldsymbol{\mu}_p, \boldsymbol{\Sigma}_p)$ . Remarkably,  $\boldsymbol{\mu}_p$  and  $\boldsymbol{\Sigma}_p$  are available in closed-form expressions.

In the following, we assess the forced response of annual and global mean total precipitable water (GTPW), as well as the response to specific subsets of radiative forcings (attribution). These forced responses are then constrained by GMST (a good surrogate for GSAT) and/or by observations and reanalyses of GTPW.

Therefore, we consider the following CMIP matrix:

$$\mathbf{x} = (\mathbf{T}_{\text{all}}, \mathbf{W}_{\text{all}}, \mathbf{W}_{\text{ghg}}, \mathbf{W}_{\text{nat}}),$$

where each element is an entire 1850-2100 time-series of the forced response,  $\mathbf{T}$  and  $\mathbf{W}$  stand for GSAT and GTPW, respectively. “all”, “ghg” or “nat” are the subsets of external forcings considered. Similarly, we define an observed matrix as:

$$\mathbf{y} = (\mathbf{T}_{\text{obs}}, \mathbf{W}_{\text{obs}}),$$

i.e., only observed time-series are used in  $\mathbf{y}$ . The length of these time-series varies: 1850-2021 for GMST, 1994-2021 for GTPW. As a result,  $\mathbf{x}$  is a very long vector, and all attribution or projection diagnoses presented below can be derived from the posterior distribution  $p(\mathbf{x}|\mathbf{y})$ . Following Ribes et al. (2021),  $\boldsymbol{\mu}_x$  and  $\boldsymbol{\Sigma}_x$  are estimated as the sample mean and covariance of the forced responses.  $\boldsymbol{\Sigma}_y$  requires statistical modelling of internal variability and measurement errors, and we use a mix of auto-regressive processes of order 1 (AR1) to model internal climate variability. The intrinsic variance of both GMST and GTPW is derived from observations after subtracting the multi-model mean estimate of the forced response of GSAT and GTPW respectively. We also assume a dependence between GMST and GTPW internal variability, by accounting for the correlation between the two residuals in  $\boldsymbol{\Sigma}_y$ . The assessment of measurement uncertainty is based on the HadCRUT5 ensemble for GMST (200 members), while for GTPW, we use three global atmospheric reanalyses in addition to the *in situ* GNSS measurements: ERA5, JRA55 and MERRA-2.

## References:

- 425 1. Held, I.M., Soden, B.J. Robust Responses of the Hydrological Cycle to Global Warming. *J. Climate*, **19**, 5686-5699 (2006).
2. Allan, R.P., Byrne, M., Cherchi, A., Douville, H., Fowler, H., Ghan, T., Swann, A., Zolina, O. Advances in understanding large-scale responses of the water cycle to climate change. *Annals of the New York Academy of Sciences*, doi:10.1111/nyas.14337 (2020).
- 430 3. Douville, H., et al. In Climate Change 2021: The Physical Science Basis. *Contribution of Working Group I to the Sixth Assessment Report of the Intergovernmental Panel on Climate Change*, **Chapter 8**, Cambridge University Press (2021).
4. Fischer, E.M., Knutti, R. Observed heavy precipitation increase confirms theory and early models. *Nat. Clim. Change*, **6**, 986-991, doi:10.1038/NCLIMATE3110 (2016).
- 435 5. John, A., Douville H., Ribes A., Yiou P. CMIP6 model uncertainties in extreme precipitation projections. *Weather and Climate Extremes* (revised, 2022).
6. O’Gorman, P.A., Muller, C.J. How closely do changes in surface and column water vapor follow Clausius–Clapeyron scaling in climate change simulations. *Environ. Res. Lett.*, **5**, 025207 (2010).
- 440 7. Climate Change 2021: The Physical Science Basis. *Contribution of Working Group I to the Sixth Assessment Report of the Intergovernmental Panel on Climate Change* [Masson-Delmotte, V., et al. (eds.)]. Cambridge University Press (2021).
8. Vial, J., Dufresne, J.L., Bony, S. On the interpretation of inter-model spread in CMIP5 climate sensitivity estimates. *Clim. Dyn.*, **41**, 3339–3362, doi :10.1007/s00382-013-1725-9 (2013).
- 445 9. Schröder, M., et al. The GEWEX Water Vapor Assessment: overview and introduction to results and recommendations. *Remote Sens.*, **11**, 25 (2019).
10. Bosilovich, M.G., Robertson, F.R., Takacs, L., Molod, A., Mocko, D. Atmospheric Water Balance and Variability in the MERRA-2 Reanalysis. *J. Climate*, **30**, 1177–1196 (2017).

- 450 11. Santer, B.D. et al. Identification of human-induced changes in atmospheric moisture content. *Proc. Nat. Am. Soc.*, **104**, 15248–15253 (2007).
12. Chung, E-S., Soden, B., Sohn B.J., Shi, L. Upper-tropospheric moistening in response to anthropogenic warming. *Proc. Nat. Am. Sc.*, **111**, 11636-11641 (2014).
13. Willett, K.M., Gillett, N.P., Jones, P.D., Thorne, P.M. Attribution of observed surface  
455 humidity changes to human influence. *Nature*, **449**, doi:10.1038/nature06207 (2007).
14. Douville, H., Plazzotta, M. Midlatitude summer drying: An underestimated threat in CMIP5 models? *Geophys. Res. Lett.*, **44**, 9967-9975 (2017).
15. Eyring, V., et al. In Climate Change 2021: The Physical Science Basis. *Contribution of Working Group I to the Sixth Assessment Report of the Intergovernmental Panel on  
460 Climate Change, Chapter 3*, Cambridge University Press (2021).
16. Bevis, M., Businger, S., Chiswell, S., Herning, T. A., Anthes, R. A., Rocken, C., Ware, R. H. GPS Meteorology: Mapping zenith wet delay onto precipitable water. *J. Appl. Meteor.*, **33**, 379–386 (1994).
17. Bock, O. and Parracho, A. C. Consistency and representativeness of integrated water  
465 vapour from ground-based GPS observations and ERA-Interim reanalysis, *Atmos. Chem. Phys.*, **19**, 9453–9468 (2019).
18. Dow, J.M., Neilan, R.E. & Rizos, C. The International GNSS Service in a changing landscape of Global Navigation Satellite Systems. *J. Geod.*, **83**, 191–198 (2009).
19. Paracho, A.C., Bock, O., Bastin, S. Global IWV trends and variability in atmospheric  
470 reanalyses and GPS observations. *Atmos. Chem. Phys.*, **18**, 16213-16237 (2018).
20. Bock, O. Global GNSS Integrated Water Vapour data, 1994-2021 [Data set]. AERIS. <https://doi.org/10.25326/68> (2022).
21. Poli, P., et al. ERA-20C: An Atmospheric Reanalysis of the Twentieth Century, *Journal of Climate*, 29(11), 4083-4097 (2016).
- 475 22. Gillett, N.P., et al. Detection and Attribution Model Intercomparison Project (DAMIP). *Geosci. Model Dev. Discuss.*, **9**, 3685–3697 (2016).
23. Liepert, B. et al., Can aerosols spin down the water cycle in a warmer and moister world? *Geophys. Res. Lett.*, **31**, L06207 (2004).

- 480 24. Ribes, A., Qasmi, S., Gillett, N. Making climate projections conditional on historical observations. *Sc. Adv.*, **7**, eabc0671 (2021).
25. Qasmi, S., Ribes, A. Reducing uncertainty in local climate projections (in review, <https://doi.org/10.21203/rs.3.rs-364943/v3>)
- 485 26. Knutti, R., Sedláček, J., Sanderson, B. M., Lorenz, R., Fischer, E. M., Eyring, V. A climate model projection weighting scheme accounting for performance and interdependence, *Geophys. Res. Lett.*, **44**, 1909–1918 (2017).
27. Han, Y., Zhang, M-Z., Xu, Z., Guo, W. Assessing the performance of 33 CMIP6 models in simulating the large-scale environmental fields of tropical cyclones. *Clim. Dyn.*, **58**, 1683–1698 (2022).
- 490 28. Trent, T., Schröder, M, Remedios, J. GEWEX water vapor assessment: Validation of AIRS tropospheric humidity profiles with characterized radiosonde soundings *Journal Geophys. Res.: Atmos.*, **124**, 886–906 (2019).
29. Po-Chedley, S., Zelinka, M. D., Jeevanjee, N., Thorsen, T. J., Santer, B. D. Climatology explains intermodel spread in tropical upper tropospheric cloud and relative humidity response to greenhouse warming. *Geophys. Res. Lett.*, **46**, 13,399–13,409 (2019).
- 495 30. Moseid, K.O., M. Schulz, M., Storelvmo, T., Julsrud, I.R., Olivié, D., Nabat, P., Wild, M., Cole, J.N.S., Takemura, T., Oshima, N., Bauer, S.E., Gastineau, G. Bias in CMIP6 models as compared to observed regional dimming and brightening. *Atmos. Chem. Phys.*, **20**, no. 24, 16023-16040 (2020).

500 **Corresponding author:** Correspondence or requests should be addressed to  
Dr. Hervé Douville, CNRM/GMGEC/AMACS, 42 avenue Coriolis, 31057 Tou-  
louse Cedex, France. E-mail: herve.douville@meteo.fr

**Acknowledgements:** The authors are grateful to all global modelling centres  
505 which have contributed to CMIP5 and CMIP6, as well as to the people in charge  
of the ESGF archive (<https://esgf-node.llnl.gov/projects/>) and of the ESPRI plat-  
form (<https://mesocentre.ipsl.fr/plate-forme-physique/>). The study has been  
partly supported by the European Union's Horizon 2020 research and innova-  
tion program under the EUCP (Grant Agreement 776613) and the CONSTRAIN  
510 (Grant Agreement 820829) projects.

**Author contributions:** H.D. designed the research, processed the CMIP5 and  
CMIP6 datasets, produced all figures except Fig. 1 and drafted the first manu-  
script; O.B. processed the GNSS measurements and the atmospheric reanal-  
515 yses and produced Fig. 1; A.R. and S.Q. developed the KCC statistical pack-  
ages, everyone participated in the writing of the submitted manuscript.

**Data and script availability:** CMIP5 and CMIP6 data are available on the  
ESGF archive at <https://esgf-node.llnl.gov/>, GNSS data are available at  
520 <https://en.aeris-data.fr/>, the KCC statistical package for observational constraint  
is available on gitlab at <https://gitlab.com/saidqasmi/KCC>, scripts used to plot  
the figures are available upon request from the corresponding author.

### Figure captions:

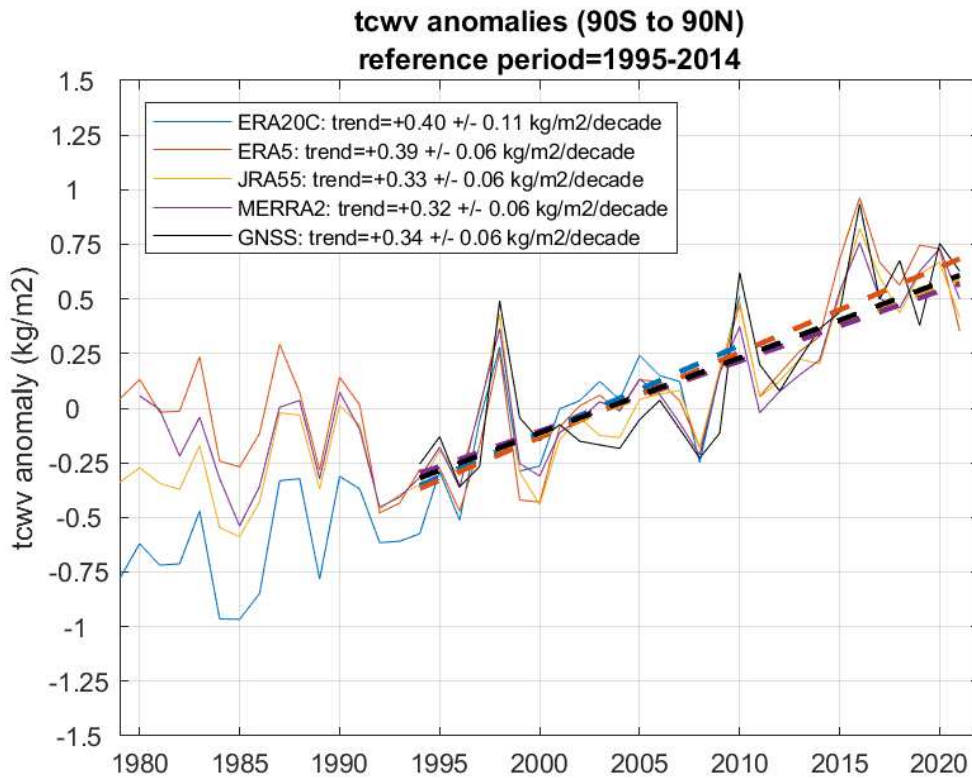
525 Figure 1: Annual mean timeseries (1980-2021) of global mean total precipita-  
ble water (GTPW) from GNSS *in situ* measurements of GPS reception and  
from four global atmospheric re-analyses (ERA5, ERA20C, JRA55 and  
MERRA-2). Anomalies have been estimated against the 1995-2014 reference  
530 climatology, except for ERA20C (1995-2010) which does not extend beyond  
2010. Linear trends have been estimated over the 1994-2021 period (only  
1994-2010 for ERA20C).

Figure 2: Annual mean timeseries (1850-2020) of global mean anomalies of  
total precipitable water (GTPW) from four sets of historical experiments using a  
535 subset of eight CMIP6 models with at least three realization for each set of  
experiment driven by individual anthropogenic (GHG, AER) or natural (NAT)  
radiative forcings or their combination (ALL). ERA20C (crosses) and GNSS (tri-  
angles) anomalies are also shown as observational references. All anomalies  
are estimated relative to the 1900-1929 baseline period. Since GNSS meas-  
540 urements are only available since 1994, the anomalies shown in Fig. 1 have  
been shifted using the 1995-2014 minus 1900-1929 climatological differences  
from the historical simulations with ALL forcings.

Figure 3: Mean (solid lines) and 5-95% range (shading) of the prior and poste-  
545 rior distributions of the forced GTPW annual mean response to both natural and  
anthropogenic radiative forcings in historical simulations and SSP5-8.5

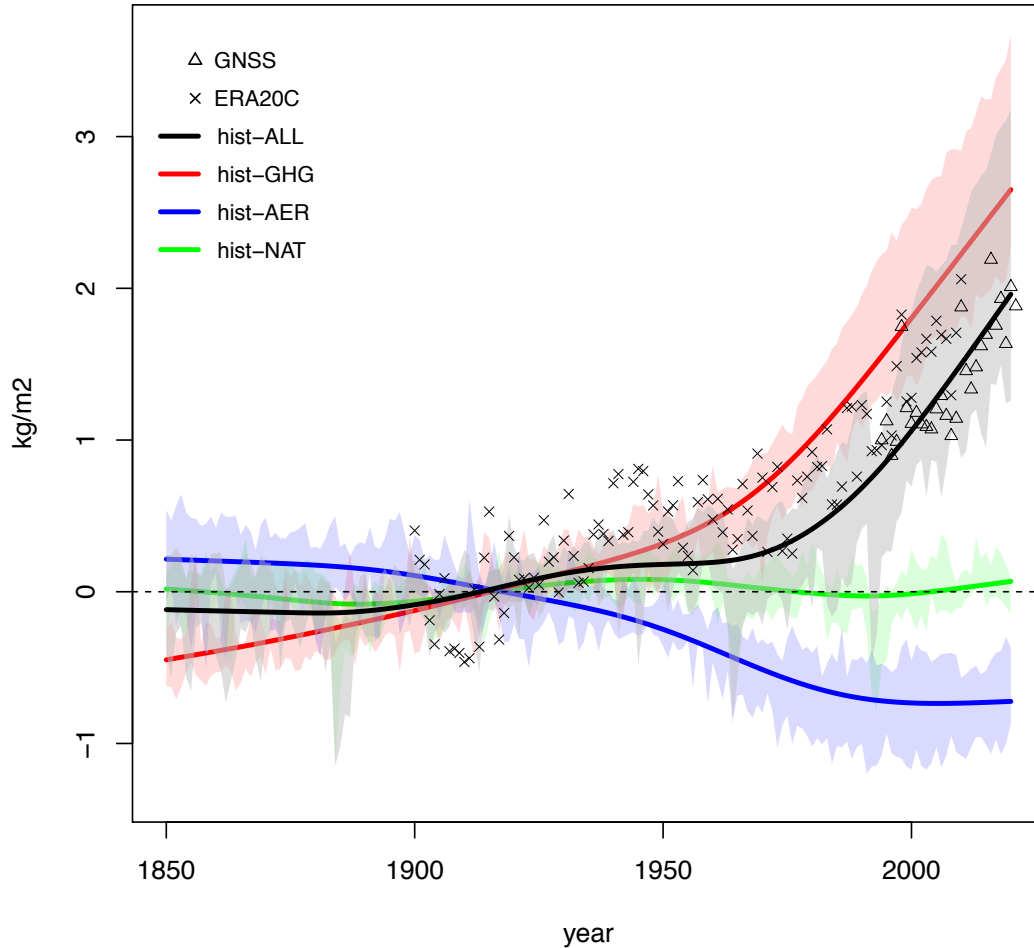
projections from 28 CMIP6 models: a) KCC using the GMST-only observational constraint; b) KCC using the GTPW-only observational constraint; c) KCC using both observational constraints; d) Regression based on the GSAT posterior distribution and an observed  $7\%/^{\circ}\text{C}$  regression coefficient as derived from GNSS and GMST observations (see text). After the constraint, the 5-95% interval at the end of the 21<sup>st</sup> century is reduced by 34%, 10%, 39% and 23% in panel a, b, c, and d respectively. In all panels, the dashed green line shows the ensemble mean GTPW change estimated when applying a simple scaling (see Methods) of the ensemble mean forced GSAT response. The mean observed anomalies are shown as black (gray) filled circles when they are (not) used for constraining the model response.

Figure 4: Scatterplot of recent trends in GTPW (%) versus GSAT (K). Linear trends are estimated over the 1994-2021 period where both observed estimates of GMST and GTPW are available. Individual CMIP6 models are shown as cyan crosses while the ensemble mean and ensemble spread of their *prior* and *posterior* distributions are shown as crosses and ellipses in blue and red respectively. Observed trends and related uncertainties are shown in black. The grey dotted lines denote three illustrative rates of increase ranging from  $6\%/^{\circ}\text{C}$  to  $8\%/^{\circ}\text{C}$ .

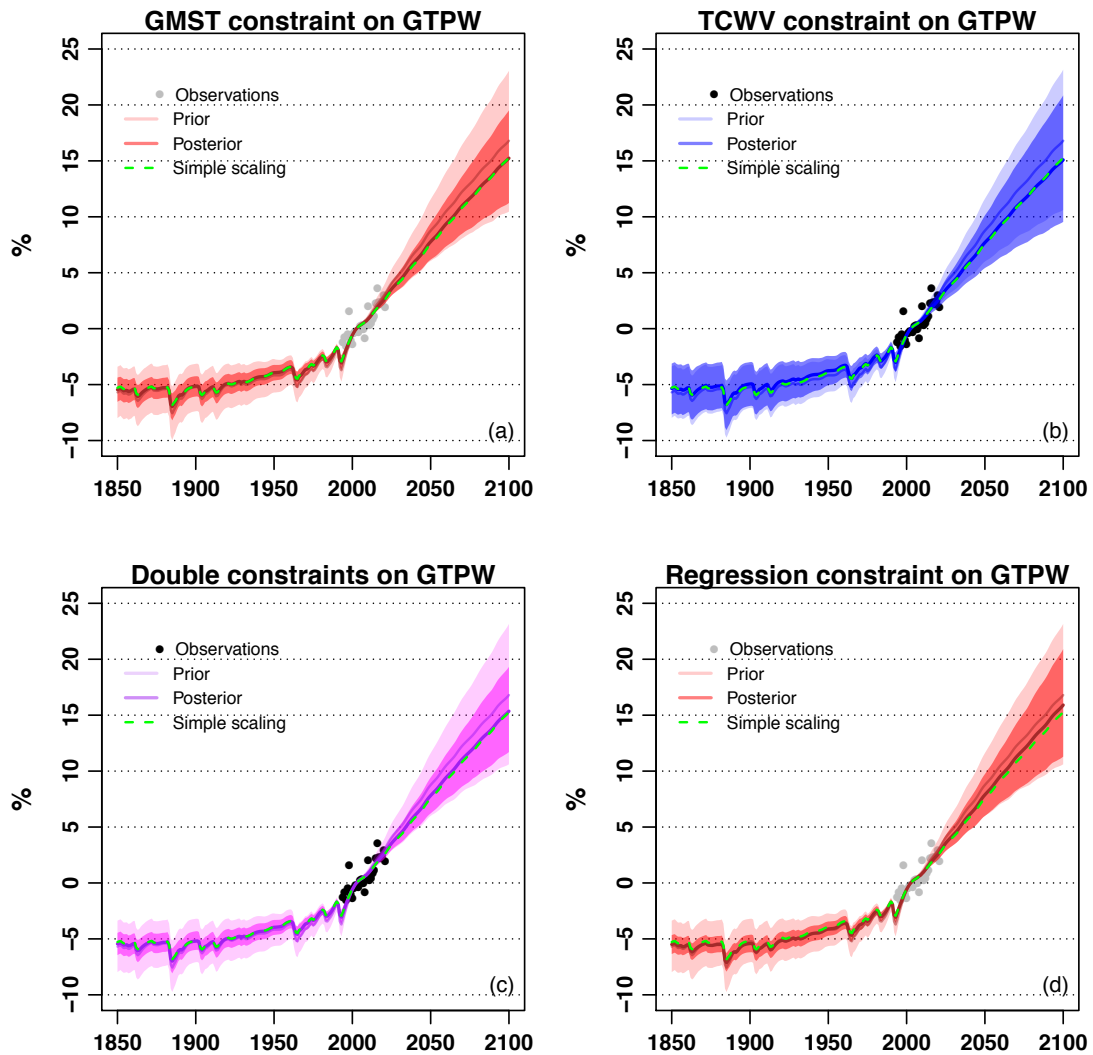


575 Figure 1: Annual mean timeseries (1980-2021) of global mean total precipita-  
 ble water (GTPW) from GNSS *in situ* measurements of GPS reception and  
 from four global atmospheric re-analyses (ERA5, ERA20C, JRA55 and  
 MERRA-2). Anomalies have been estimated against the 1995-2014 reference  
 580 climatology, except for ERA20C (1995-2010) which does not extend beyond  
 2010. Linear trends have been estimated over the 1994-2021 period (only  
 1994-2010 for ERA20C).

**Simulated changes in GTPW  
versus observed changes in TCWV averaged over the globe**



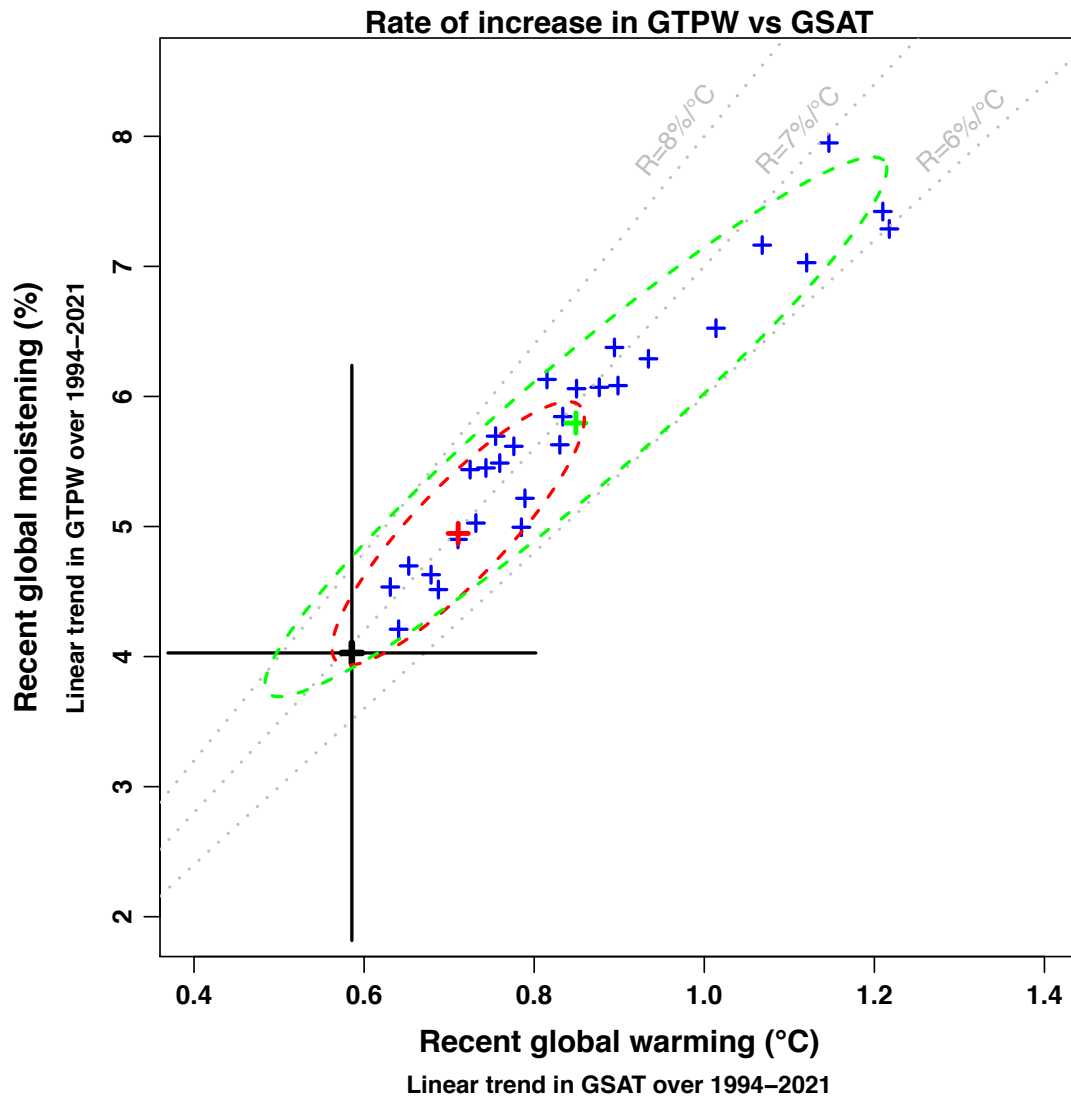
585 Figure 2: Annual mean timeseries (1850-2020) of global mean anomalies of  
total precipitable water (GTPW) from four sets of historical experiments using a  
subset of eight CMIP6 models with at least three realization for each set of  
experiment driven by individual anthropogenic (GHG, AER) or natural (NAT)  
radiative forcings or their combination (ALL). ERA20C (crosses) and GNSS (tri-  
590 angles) anomalies are also shown as observational references. All anomalies  
are estimated relative to the 1900-1929 baseline period. Since GNSS meas-  
urements are only available since 1994, the anomalies shown in Fig. 1 have  
been shifted using the 1995-2014 minus 1900-1929 climatological differences  
from the historical simulations with ALL forcings.



595

Figure 3: Mean (solid lines) and 5-95% range (shading) of the prior and posterior distributions of the forced GTPW annual mean response to both natural and anthropogenic radiative forcings in historical simulations and SSP5-8.5 projections from 28 CMIP6 models: a) KCC using the GMST-only observational constraint; b) KCC using the GTPW-only observational constraint; c) KCC using both observational constraints; d) Regression based on the GSAT posterior distribution and an observed  $7\%/^{\circ}\text{C}$  regression coefficient as derived from GNSS and GMST observations (see text). After the constraint, the 5-95% interval at the end of the 21<sup>st</sup> century is reduced by 34%, 10%, 39% and 23% in panel a, b, c, and d respectively. In all panels, the dashed green line shows the ensemble mean GTPW change estimated when applying a simple scaling (see Methods) of the ensemble mean forced GSAT response. The mean observed anomalies are show as black (gray) filled circles when they are (not) used for constraining the model response.

610



615 Figure 4: Scatterplot of recent trends in GTPW (%) versus GSAT (K). Linear  
 trends are estimated over the 1994–2021 period where both observed estimates  
 of GMST and GTPW are available. Individual CMIP6 models are shown as cyan  
 crosses while the ensemble mean and ensemble spread of their *prior* and *pos-*  
*terior* distributions are shown as crosses and ellipses in blue and red respec-  
 620 tively. Observed trends and related uncertainties are shown in black. The grey  
 dotted lines denote three illustrative rates of increase ranging from 6%/°C to  
 8%/°C.

## Supplementary Files

This is a list of supplementary files associated with this preprint. Click to download.

- [Supplementarysubmitted.pdf](#)